

Parity anomaly cancellation in a three-dimensional QED with single massless Dirac fermion

Nikhil Karthik^{1,*} and Rajamani Narayanan^{2,†}

¹*Physics Department, Brookhaven National Laboratory,
Upton, New York 11973-5000, USA*

²*Department of Physics, Florida International University, Miami, FL 33199*

(Dated: June 29, 2018)

Abstract

We study a three-dimensional non-compact QED with a single two-component massless fermion and two infinitely massive regulator fermions of half the charge using lattice overlap formalism. The parity anomaly is expected to cancel exactly between the massless and regulator fermions in the continuum, but this cancellation is inexact on lattice akin to lattice chiral gauge theories. We show non-perturbatively that parity-breaking terms vanish in the continuum limit at any finite volume. We present numerical evidences that the resulting parity-invariant theory spontaneously breaks parity in the infinite volume limit.

* nkarthik@bnl.gov

† rajamani.narayanan@fiu.edu

I. INTRODUCTION

The standard model of particle physics is anomaly free due to an exact non-trivial cancellation of gauge anomalies [1] from different representations to all orders of perturbation theory. Chiral anomalies outside perturbation theory can be discussed geometrically [2] and the relation between consistent and covariant currents [3] plays a central role. Such fundamental issues should be addressed in any non-perturbative formalism of chiral gauge theories. Overlap formalism of chiral gauge theories on the lattice [4] was motivated [5] by an attempt to regularize a specific chiral gauge theory using infinite number of Pauli-Villars fields [6] and the ability to use domain walls to create a chiral zero mode [7]. In order to discuss the problem of chiral anomalies in a gauge covariant and geometric manner, a two-form in the space of gauge fields defined through the curl of the difference between the covariant and consistent currents was introduced within the overlap formalism in [8], and it was identified to be the Berry's curvature. Two sources contribute to this Berry's curvature for a chiral fermion in an anomalous representation – the first is due to the genuine continuum gauge anomaly that cannot be removed, and the second is due to the spatial smearing of the anomalous contribution due to finite lattice spacing. There is just the contribution due to smearing in an anomaly free chiral theory which can only be removed by fine-tuning the irrelevant terms in fermion action on the lattice [8]. The exceptions to the fine-tuning are QCD-like vector theories where the anomaly cancellation is trivial.

The odd-dimensional analog to chiral anomalies is parity anomaly [9–12] and this also can be discussed geometrically [13]. In this letter, we consider a three-dimensional analog to the chiral gauge theories, where there is a non-trivial cancellation of parity anomaly between massless fermions and infinitely massive fermions, which is a property unique to three-dimensions. The theory we consider is an Abelian $U(1)$ gauge theory with one massless Dirac fermion of charge q and two infinitely massive fermions of charges $\frac{q}{2}$ in a three-torus with physical size, ℓ^3 . This corresponds to the Euclidean continuum theory, with an implicit regularization,

$$\mathcal{L} = \bar{\psi} (\not{\partial} + iq\not{A}) \psi - \frac{q^2 i}{8\pi} \epsilon_{\mu\nu\rho} A_\mu \partial_\nu A_\rho + \frac{1}{4} F_{\mu\nu} F^{\mu\nu}, \quad (1)$$

written in standard notation in units where the coupling constant $g^2 = 1$. This theory has phenomenological relevance to the low-energy physics of fractional quantum Hall effect at half-filled Landau level [14–16]. Like in even dimensions, lattice regularization of this theory

within the overlap formalism [4, 17, 18] does not succeed in an exact cancellation of the parity anomaly. A salient result in this letter is the numerical evidence for the restoration of parity invariance in the continuum at any finite physical volume without the need for fine-tuning the fermion action, which suggests a similar situation to hold in even dimensional chiral gauge theories as anticipated in [8]. This will also establish the existence of such three-dimensional theories outside perturbation theory. We will then present a numerical study of this theory in the infinite volume limit and provide evidence for spontaneous breaking of parity.

II. MODUS OPERANDI

As is standard in lattice field theory, we discretize the physical volume ℓ^3 using L^3 lattice points with the lattice spacing being $\frac{\ell}{L}$. The continuum limit is achieved by taking the $L \rightarrow \infty$ limit at fixed value of ℓ . For the Abelian theory, the dynamical real lattice variables are $\theta_\mu(\mathbf{n})$ at the link connecting the lattice point at \mathbf{n} to $\mathbf{n} + \hat{\mu}$. The lattice regularized partition function of the model in Eq. (1) using the overlap formalism [17, 18] is

$$Z(\ell, L) = \int [d\theta] e^{-S_g(\theta)} \det \left(\frac{1 + V_\theta}{2} \right) \det^2 V_{\frac{1}{2}\theta}^\dagger, \quad (2)$$

where $S_g(\theta)$ is the non-compact gauge action on the lattice (obtained by discretizing the $F_{\mu\nu}^2$ term). The unitary operator $V_{q\theta}$ depends on the compact link variables $U_\mu^q(\mathbf{n}) = e^{iq\theta_\mu(\mathbf{n})}$ where q is the charge of the fermion coupled to the gauge field. We have set $q = 1$ in Eq. (1) and the first determinant factor realizes the effective action obtained by integrating out the massless fermion in Eq. (1) and the second determinant factor realizes the Chern-Simons term in Eq. (1) as induced by an infinitely massive fermion.

If we define the induced action $2\mathcal{A}_q$ from the infinite mass fermion via, $\det V_{q\theta} \equiv \exp(2iq^2\mathcal{A}_q)$, then we expect $\mathcal{A}_q(\theta)$ to be independent of q for smooth gauge fields [11, 12, 19, 20], and be the same as the level-one Chern-Simons action. If we perform the Euclidean parity transformation, under which $V_{q\theta} \rightarrow V_{q\theta}^\dagger$, the path integral in Eq. (2) transforms to

$$Z(\ell, L) = \int [d\theta] e^{-S_g(\theta)} \det \frac{1 + V_\theta}{2} \det^2 V_{\frac{1}{2}\theta}^\dagger e^{-2i\mathcal{A}(\theta)}, \quad (3)$$

where

$$\mathcal{A}(\theta) = \mathcal{A}_1(\theta) - \mathcal{A}_{\frac{1}{2}}(\theta). \quad (4)$$

Parity anomaly cancellation in the continuum means that $2\mathcal{A} = 0$ or equivalently, $\mathcal{A} = n\pi$ for $n = 0, \pm 1$ as $L \rightarrow \infty$. On the lattice however, the non-trivial anomaly cancellation between two different charges will result in $2\mathcal{A}(\theta)$ being zero only on classically smooth backgrounds. An ensemble of gauge field configurations on the lattice away from the continuum limit will not be smooth and we do not expect $2\mathcal{A}(\theta) = 0 \pmod{2\pi}$, leading to

$$\det \frac{1 + V_\theta}{2} \det^2 V_{\frac{1}{2}\theta}^\dagger = \left| \det \frac{1 + V_\theta}{2} \right| e^{i\mathcal{A}(\theta)}; \quad \mathcal{A} \in (-\pi, \pi], \quad (5)$$

which forms the core of the problem addressed in this letter.

Our strategy can be summarized as follows. Using the Rational Hybrid Monte Carlo (RHMC) [21–23], an algorithm based on molecular dynamics evolution, we numerically simulate the theory on the lattice using the positive definite measure

$$p_+(\theta) = \left| \det \frac{1 + V_\theta}{2} \right| e^{-S_g}, \quad (6)$$

and consider the phase $e^{i\mathcal{A}}$ to be part of the observables. Our first aim is to study the distribution of \mathcal{A} generated at a given ℓ and L and show that the distribution has a tendency to approach a delta function for all ℓ as we take $L \rightarrow \infty$. As the lattice spacing increases with ℓ in a range of numerically feasible values of L , we can only provide reasonable numerical evidence for parity anomaly cancellation over a limited but wide range of ℓ . Our second aim in this letter is to assume that parity anomaly cancellation holds for all values of ℓ and study the infrared physics of the model in Eq. (1) using $p_+(\theta)$ as the measure.

III. ANOMALY CANCELLATION

Figure 1 shows the distribution $P(\mathcal{A})$ of $\mathcal{A}(\theta)$ as sampled using $p_+(\theta)$ in three panels, top to bottom, for $\ell = 4, 32, 200$ respectively. Within each panel for a fixed ℓ , the different symbols correspond to different lattice spacings. Due to the parity-invariant measure $p_+(\theta)$, the distributions are almost symmetric with small deviations resulting from finite statistics. We notice from the $\ell = 4$ and 32 panels that $P(\mathcal{A})$ gets sharper as one approaches the continuum limit $L \rightarrow \infty$. However, this approach of the width of the distribution to zero is hard to see in the $\ell = 200$ panel, and it is understandable since the finest lattice spacing ($L = 16$) at $\ell = 200$, where we were able to compute \mathcal{A} is 5.4 times larger than the one at $\ell = 32$ ($L = 14$). By putting together the data for \mathcal{A} from all ℓ and L , we now justify that

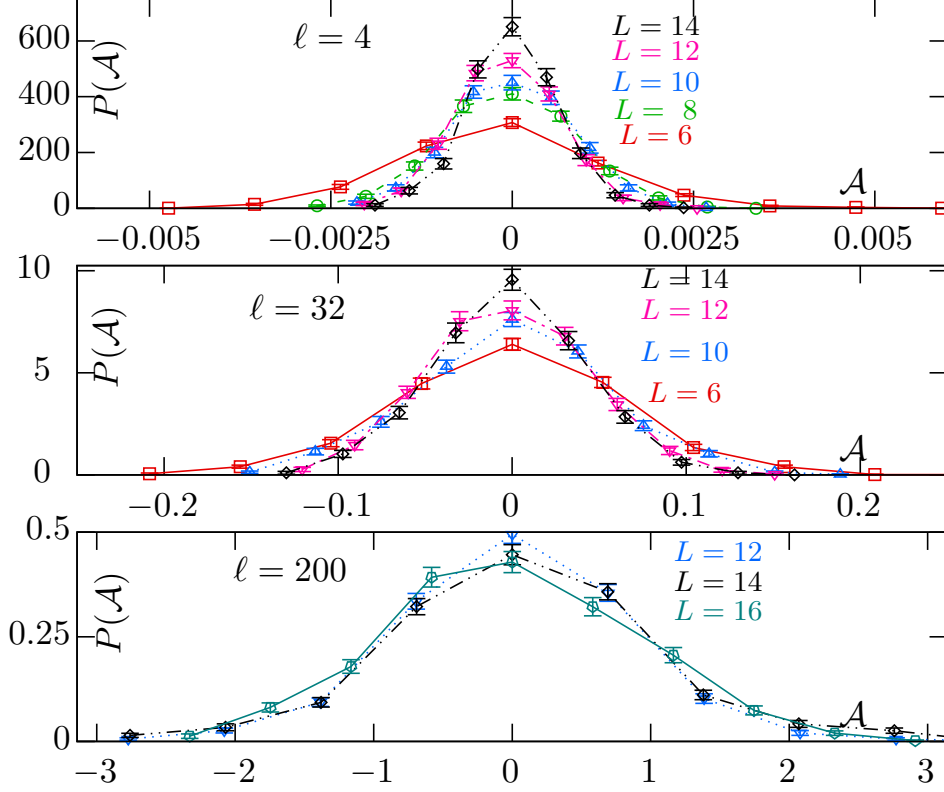


FIG. 1. The distribution of $\mathcal{A}(\theta)$ at different physical volumes ℓ^3 are shown in the three panels. The different symbols correspond to different L .

the distributions at larger ℓ will indeed get sharper at prohibitively large values of L . Since one expects the remnant phase \mathcal{A} to be a volume integral of local irrelevant terms, we show the variance per unit physical volume, $\ell^{-3}\text{Var}(\mathcal{A})$, as a function of lattice spacing, ℓ/L , in the left panel of Figure 2. The data points of same colored symbol belong to a fixed value of ℓ but differ in L , while different colored symbols correspond to different ℓ as specified near them. The data approximately falls on a universal curve, with $\text{Var}(\mathcal{A}) \sim L^{-1}$ at smaller ℓ/L . On the right panel of Figure 2, we show the scaled peak-height of the distribution, $\ell^{3/2}P(\mathcal{A} = 0)$, as a function of ℓ/L . The approximate data collapse suggests a \sqrt{L} increase in the peak-height at smaller ℓ/L . As expected, higher order effects in lattice spacing come into play in both figures for larger $\frac{\ell}{L}$. Based on these empirical observations, we find reasonable evidence for $P(\mathcal{A})$ to approach a delta function in the continuum limit at a fixed ℓ and it is important that one takes the continuum limit before taking the infinite volume limit.

We now discuss the sign of the fermion determinant. The distribution $P(\mathcal{A})$ on the

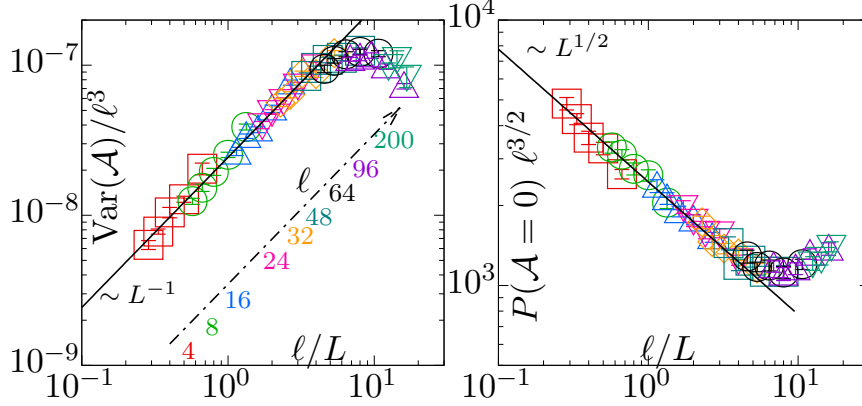


FIG. 2. The variance (left panel) and the height of the distribution at $\mathcal{A} = 0$ (right panel) for $P(\mathcal{A})$, both scaled by appropriate powers of ℓ , are shown as functions of lattice spacing.

coarser lattices, such as the one at $\ell = 200$, covers the entire range $(-\pi, \pi]$, but still remains peaked at zero. Based on the arguments above, this implies that the distribution in the continuum limit will be peaked around zero, in spite of values of \mathcal{A} close to π being allowed in the essentially continuous molecular dynamics evolution of gauge fields used by the RHMC algorithm on coarser lattices. In principle, we could have found a separation of our ensemble into two sectors on coarser lattice spacings (corresponding to $\mathcal{A}(L = \infty) = 0$ and $\pm\pi$) easily identified by a doubly peaked $P(\mathcal{A})$. In this case, it would have been necessary to have a zero of the fermion determinant along the RHMC's canonical evolution as the continuum limit is approached. Since we did not find this to be the case, our result is consistent with the absence of topological zero modes in odd-dimensional space without a boundary [24, 25]. In this manner, we have succeeded in demonstrating that Eq. (2) has a parity invariant as well as an effectively positive measure in the continuum.

Another quantity relevant to the anomaly cancellation is

$$J_i^q(\mathbf{n}) = \frac{\delta}{\delta\theta_i(\mathbf{n})} \mathcal{A}_q(\theta), \quad (7)$$

which is a fermion-induced pseudo-vector current in lattice units, and the expectation value of its magnitude is $E_q(\mathbf{n}) = \langle \mathbf{J}^q(\mathbf{n}) \cdot \mathbf{J}^q(\mathbf{n}) \rangle_+$. One expects $J_i^q(\mathbf{n})$ to depend locally on the flux $\sim \epsilon_{ijk} \Delta_j \theta_k$, but need not be ultra-local and get smeared around \mathbf{n} as discussed in [8]. In the absence of such an ultra-locality, $E(\mathbf{n}) = E_1(\mathbf{n}) - E_{1/2}(\mathbf{n})$ will not vanish at finite lattice spacing but it must vanish faster than $E_1(\mathbf{n})$ and $E_{1/2}(\mathbf{n})$ as one approaches the continuum. In Figure 3, we put together the data from all ℓ and L for E_1 and $E_{1/2}$ at an arbitrarily

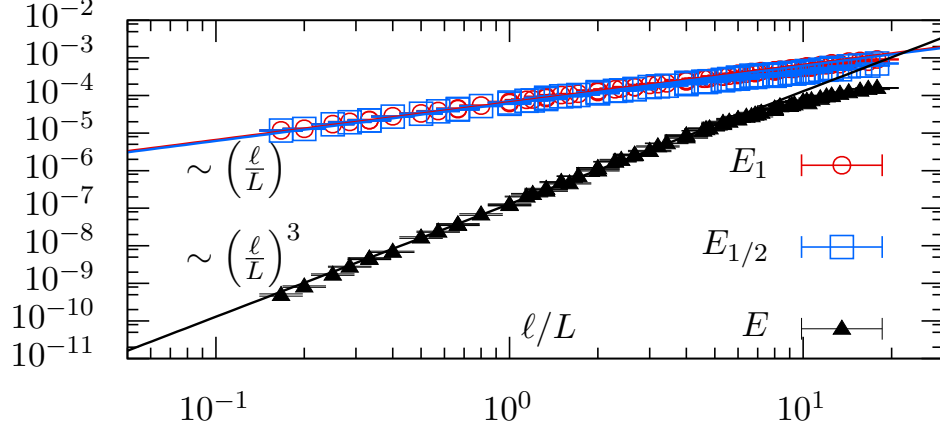


FIG. 3. The dependence of E_1 , $E_{1/2}$ and their difference, E , on lattice spacing ℓ/L .

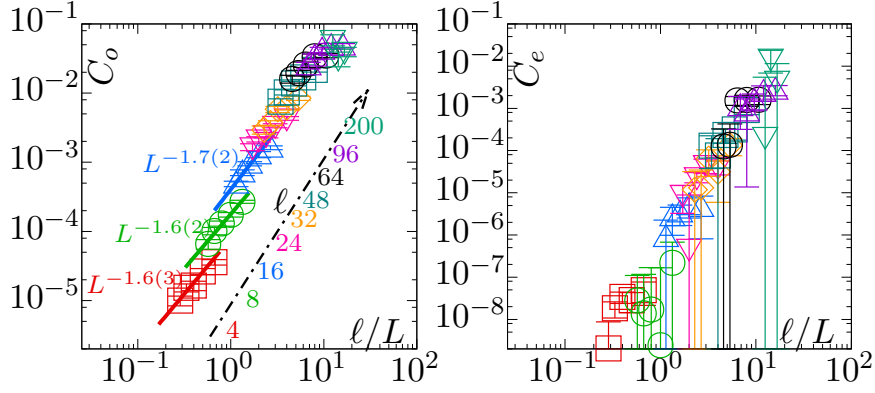


FIG. 4. The approach of C_o (left) and C_e (right) to 0 in the continuum limit.

chosen \mathbf{n} , and show it as a function of lattice spacing $\frac{\ell}{L}$. The data from different values of ℓ fall on the same curve due to the local nature of this observable. The lattice spacing scaling of E_1 and $E_{1/2}$ is $\frac{\ell}{L}$, the same as the average local energy density. With this combined data, we see that E falls off with the lattice spacing like $(\frac{\ell}{L})^3$, faster than E_1 or $E_{1/2}$ by two powers of lattice spacing ensuring again that the theory will be parity-invariant at all values of ℓ studied here.

Having demonstrated the path integral measure is anomaly free in the continuum limit, it is also imperative that we show the VEVs of parity-odd observables vanish in the continuum limit. Decomposing any observable \mathcal{O} into its parity-even and odd components \mathcal{O}_e and \mathcal{O}_o

respectively, its expectation value can be written as

$$\langle \mathcal{O}(\theta) \rangle = \frac{\langle \mathcal{O}_e(\theta) \cos \mathcal{A}(\theta) \rangle_+}{\langle \cos \mathcal{A}(\theta) \rangle_+} + i \frac{\langle \mathcal{O}_o(\theta) \sin \mathcal{A}(\theta) \rangle_+}{\langle \cos \mathcal{A}(\theta) \rangle_+}. \quad (8)$$

We want to show that in the continuum limit, the parity-even first term on the right hand side becomes $\langle \mathcal{O}_e \rangle_+$ and the parity-odd second term vanishes. We consider the correction $C_e + iC_o = \langle \mathcal{O} \rangle - \langle \mathcal{O}_e \rangle_+$ as a function of L . For \mathcal{O} , we used the dimensionless lowest positive eigenvalue $\lambda_1^+(\theta)\ell$ of the inverse of massless Hermitian overlap Dirac propagator, $iG^{-1}(\theta)L = i\frac{1+V_\theta}{1-V_\theta}L$, at different L . In Figure 4, we show the decreasing behavior of both C_o and C_e at different fixed ℓ , as L is increased. The different colored symbols in the plot belong to different ℓ . At any finite L , C_o is significantly non-zero and indeed decreases when the lattice spacing is made smaller. On finer lattices, a distinct $L^{-\Delta}$ behavior with an empirical value $\Delta \approx 1.5$ is seen. For the data at larger ℓ/L , a downward curvature is seen implying the asymptotic values of Δ will be greater than what can be extracted from the data (which is about 1.2). On other hand, the ultra-violet physics of anomaly cancellation seems to decouple from the infra-red parity-even expectation values, as seen from the fact that C_e is much less than 0.1% of $\langle \frac{1}{2}(\lambda_1^+(\theta) + \lambda_1^+(\theta_p))\ell \rangle_+$ (and about two to three orders of magnitude lesser than the corresponding C_o) in the range of ℓ we studied. In fact, for $L > 10$, $C_e \approx 0$ within 1.5- σ error range.

IV. SPONTANEOUS SYMMETRY-BREAKING OF PARITY

Having numerically established a parity-invariant theory with a positive measure in a certain range of ℓ that was numerically accessible, we will assume this to be the case for higher values of ℓ and study the infra-red behavior of the theory by taking the $\ell \rightarrow \infty$ limit using the $p_+(\theta)$ measure. A possibility is the spontaneous symmetry breaking (SSB) of parity leading to a non-zero bilinear condensate Σ *i.e.*, at finite fermion mass m and infinite volume, $\langle \bar{\psi}\psi \rangle(m) = \Sigma \frac{m}{|m|} + O(m)$. To study this, we focus on the discrete dimensionless Dirac operator eigenvalues ordered by magnitude, $0 < \ell\lambda_1(\theta;\ell) < \ell\lambda_2(\theta;\ell) < \dots$, (which are technically obtained from $L|G^{-1}(\theta)|$), at finite ℓ . We first take the $L \rightarrow \infty$ continuum limit of $\langle \lambda_i(\ell)\ell \rangle$ (using L from 12 to 24) at different fixed ℓ ranging from 4 to 250 for this study before considering the $\ell \rightarrow \infty$ limit.

The probability distribution of $\lambda_i(\theta;\ell)$, as sampled in the Monte Carlo, will exhibit several

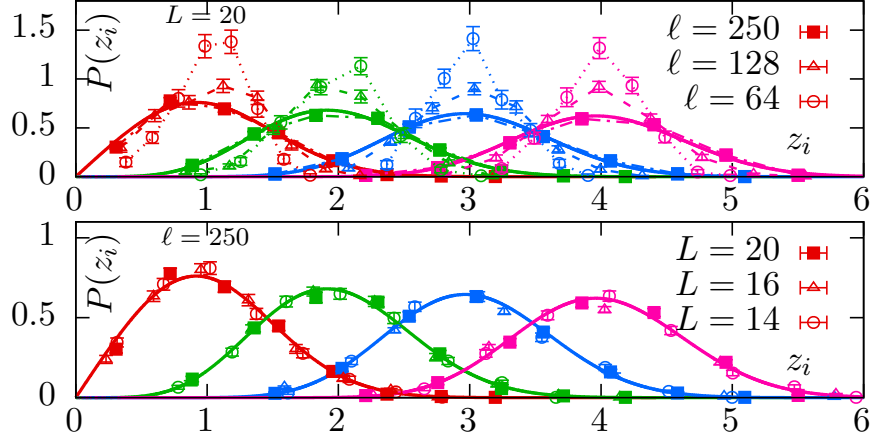


FIG. 5. Comparison of the distributions of $\lambda_i \Sigma_i(\ell) \ell^3$ (symbols connected by dotted lines), and the RMT eigenvalues z_i (solid curves). The red, green, blue and purple curves correspond to $i = 1, 2, 3, 4$ respectively. Top: volume dependence at fixed $L = 20$. Bottom: lattice spacing dependence at $\ell = 250$.

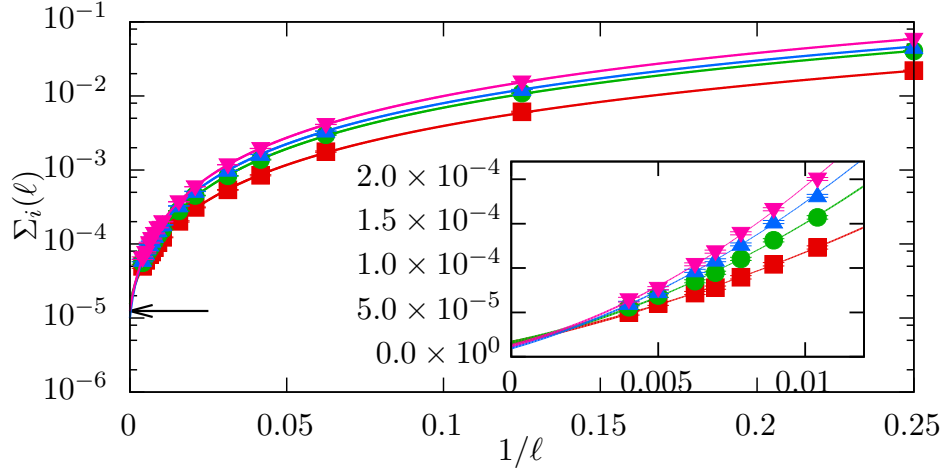


FIG. 6. The infinite volume extrapolation of $\Sigma_i(\ell)$. The red, green, blue and purple points and curves correspond to $i = 1, 2, 3, 4$ respectively.

well separated peaks consistent with a spectrum that is discrete. Perturbation theory will hold as $\ell \rightarrow 0$ and $\langle \lambda_i(\ell) \rangle$ will be proportional to ℓ^{-1} . If the theory spontaneously breaks parity as $\ell \rightarrow \infty$, then $\langle \lambda_i(\ell) \rangle \sim \ell^{-3}$ (due to a finite eigenvalue density near zero [26]) and in addition, the distributions of the individual eigenvalues should also match with those from an appropriate random matrix theory (RMT) ensemble [27–29]. If we define $\Sigma_i(\ell)$ through

the means $\langle \lambda_i(\ell) \rangle$ and z_i of the two respective distributions,

$$\langle \lambda_i(\ell) \rangle \Sigma_i(\ell) \ell^3 = z_i, \quad (9)$$

then $\Sigma_i(\ell)$ for different i should approach the same non-zero value Σ (the value of the condensate) as $\ell \rightarrow \infty$.

Figure 5 shows a comparison of the distributions of the scaled, four low-lying Dirac eigenvalues, $\ell^3 \Sigma_i(\ell, L) \lambda_i(\theta; \ell, L)$, to the distributions from the RMT, which are shown as solid curves in the plots. The top panel shows the volume dependence of the distributions at a fixed number of lattice points $L = 20$. One can see the distributions approaching the RMT as ℓ is increased from $\ell = 64$ to $\ell = 250$. The bottom panel shows this agreement between the Dirac and RMT eigenvalue distributions at $\ell = 250$ is robust as the number of lattice points L is made larger from $L = 14$ to 20. A quantitative estimate shows that the deviation of the data from the RMT distributions becomes smaller with increasing ℓ and approaches zero in the infinite volume limit. This agreement with RMT shows the presence of SSB.

Figure 6 shows $\Sigma_i(\ell)$ as extracted from the matching with RMT using Eq. (9), as a function of ℓ . The different symbols are the values of $\Sigma_i(\ell); i = 1, 2, 3, 4$ in the continuum at different fixed ℓ . At any finite ℓ the values of $\Sigma_i(\ell)$ from different i do not agree, as expected. Assuming the existence of finite non-zero value of the condensate Σ in the infinite volume limit, we used $\Sigma_i(\ell) = \Sigma_i + k_1 \ell^{-1} + k_2 \ell^{-2}$, to fit the entire range of finite ℓ data. These fits are shown by the curves. The inset magnifies the large ℓ region. We find the extrapolated values of $\Sigma_i \times 10^5$ from $i = 1, 2, 3, 4$ to be 1.5(3), 1.5(3), 1.0(2) and 1.2(2) respectively. Though the extrapolated values are about factor five smaller than the available data point, the agreement between different extrapolated values of Σ_i , together with the remarkable agreement with RMT distributions are indications of a unique $\Sigma \neq 0$ at infinite ℓ .

V. DISCUSSION

An earlier attempt [30] to verify cancellation of anomalies in a two dimensional chiral gauge theory by directly establishing gauge invariance in the continuum suffered from the fact that there is no concept of smooth gauge transformations in the continuum limit. In light of the results in this letter, it would be interesting to revisit this problem by a computation

of the continuum limit of the Berry's curvature [8] in a sequence of lattice gauge field ensembles at different lattice spacings. Of experimental relevance are the response functions of the single flavor theory studied here with the topological current coupled to a background compact gauge field ϕ , which can be realized in our lattice setup by including the term $\det [V_{\theta-\phi} V_{\theta}^{\dagger} V_{\phi}^{\dagger}]$ in Eq. (2). This particular model appears in recent discussions of duality between fermion theories [31–33]. It would be interesting to see if the SSB has any effect on the induced action for ϕ . It is trivial to extend the overlap formalism presented here for three-dimensional QED with arbitrary number of flavors (N) of massless Dirac fermions and arbitrary number of flavors (k) of infinite mass fermions. This is a numerical challenge that could benefit from the various approaches developed for the sign problem in finite density QCD.

ACKNOWLEDGMENTS

The authors would like to thank Jac Verbaarschot for a discussion on the RMT kernel. This work used the Extreme Science and Engineering Discovery Environment (XSEDE), which is supported by NSF under grant number ACI-1548562. Resources at Pittsburgh Supercomputing Center, San Diego Supercomputer Center, LSU Center for Computation and Technology and at University of Texas at Austin were used under the XSEDE allocation TG-PHY170011. Some computations in this paper were also performed on JLAB computing clusters under a USQCD type C project. R.N. acknowledges partial support by the NSF under grant number PHY-1515446. N.K. acknowledges support by the U.S. Department of Energy under contract No. de-sc0012704.

Appendix A: Details of the lattice model

We consider a symmetric periodic lattice with L points in each direction. Gauge fields on the lattice are denoted by $\theta_k(\mathbf{n}) \in \mathbb{R}$ and they are associated with the links connecting the sites \mathbf{n} and $\mathbf{n} + \hat{k}$. The fermions with charge q couple to the compact link variables

$$U_k^q(\mathbf{n}) = e^{iq\theta_k(\mathbf{n})}. \quad (\text{A1})$$

It is essential for us to include a gauge action for the Abelian field in order to be able to take the continuum limit at a fixed physical volume ℓ^3 of the torus, and have a continuum

theory free of parity anomaly. For this, we use the non-compact plaquette action given by

$$S_g(\theta) = \frac{L}{\ell} \sum_{\mathbf{n}} \sum_{j < k=1}^3 (\Delta_j \theta_k(\mathbf{n}) - \Delta_k \theta_j(\mathbf{n}))^2, \quad (\text{A2})$$

where the lattice coupling is inversely proportional to the lattice spacing $a = \frac{\ell}{L}$. Monopoles are infinite energy configurations in the continuum limit, and they are not part of the path-integral. Small values of ℓ correspond to the perturbative limit and the non-perturbative aspects of the theory can be explored by studying the asymptotic, $\ell \rightarrow \infty$, behavior of physical quantities after taking the continuum limit at a fixed ℓ . The non-compact plaquette action does not allow for non-zero net compact flux, as seen by the fermion, over any cross-section of the torus. In this case, the fermion charge q is not required to be an integer.

The regularized overlap-Dirac operator \mathcal{C}_o for a single charge q two-component fermion with a lattice mass $M \in [-1, 1]$ is given by

$$\mathcal{C}_o(M, q\theta) = \frac{(1 + M) + (1 - M)V_{q\theta}}{2}, \quad (\text{A3})$$

where $V_{q\theta} = \mathcal{C}_W(\mathcal{C}_W^\dagger \mathcal{C}_W)^{-\frac{1}{2}}$ is a unitary operator constructed out of the two-component gauge-link improved Sheikholeslami-Wohlert-Wilson-Dirac operator \mathcal{C}_W with a negative mass kept fixed in the range, $-M_W \in (0, 2)$, as one takes the continuum limit [17, 34]. An infra-red observable that we will consider later, is the spectrum of the Hermitian operator $iG^{-1} = i(1 + V_\theta)/(1 - V_\theta)$ near zero, where G is the propagator of the $q = 1$ massless overlap fermion.

Appendix B: Simulation details

We used the Rational Hybrid Monte Carlo (RHMC) algorithm [21–23] for the simulation. In this method, the gauge fields are sampled using essentially continuous molecular dynamics evolution, spoiled only by the need to use a discrete time step in the numerical evolution but rectified using accept-reject steps. All gauge field configurations along the evolution satisfy the importance sampling criterion as per the positive definite measure and statistically independent configurations are obtained by evolving for a finite time whose value is decided by the autocorrelation time.

We improved the overlap operator \mathcal{C}_o by smoothening the gauge fields θ that enter it by using one-level HYP smearing *i.e.*, instead of $U_k^q(\mathbf{n})$, we used an improved link $V_k^q(\mathbf{n}) =$

$e^{iq\theta_k^s(\mathbf{n})}$ where $\theta_k^s(\mathbf{n})$ are HYP smeared [34]. As explained in [34], this helps reducing any non-zero monopole density at finite lattice spacing. The overlap operator is constructed using the Wilson-Dirac operator \mathcal{C}_W kernel, which we improved further using the Sheikloslami-Wohler coefficient $c_{\text{sw}} = 0.5$. We fixed the Wilson mass $M_W = 1$ in \mathcal{C}_W in all our simulations.

We included the fermion contribution $|\det \mathcal{C}_o| = |\det(\frac{1+V_\theta}{2})|$ by using its pseudo-fermion representation:

$$|\det \mathcal{C}_o| = \int [d\phi] e^{-\phi^\dagger [\mathcal{C}_o^\dagger \mathcal{C}_o]^{-1/2} \phi}. \quad (\text{B1})$$

Using the standard procedure, we sampled ϕ from the above distribution by sampling Gaussian distributed complex vectors R through

$$\phi = [\mathcal{C}_o^\dagger \mathcal{C}_o]^{1/4} R. \quad (\text{B2})$$

We used the Zolotarev rational approximation (r_k, p_k) for the above fourth-root:

$$[\mathcal{C}_o^\dagger \mathcal{C}_o]^{1/4} = r_0 + \sum_{k=1}^{N_{\text{pole}}} \frac{r_k}{\mathcal{C}_o^\dagger \mathcal{C}_o + p_k}. \quad (\text{B3})$$

In the range of values for ℓ and L we used, we found the eigenvalues of $\mathcal{C}_o^\dagger \mathcal{C}_o$ to range at the most from 10^{-6} to 1. We used the Remez algorithm to obtain the poles p_k and residues r_k in the approximation with $N_{\text{pole}} = 20$, such that the error in the approximation in the range $[10^{-7}, 1]$ is bounded by 10^{-8} . We held these parameters fixed at all our simulation points.

With the usage of rational approximation, we used the standard hybrid Monte Carlo (which now becomes the rational hybrid Monte Carlo, RHMC) to sample gauge configurations — we evolved the gauge fields $\theta_i(\mathbf{n})$ and the auxiliary momenta $\pi_i(\mathbf{n})$ conjugate to the gauge field through a fictitious molecular dynamics time τ using the canonical equations of motion:

$$\begin{aligned} \frac{d}{d\tau} \theta_i(\mathbf{n}) &= \pi_i(\mathbf{n}); \\ \frac{d}{d\tau} \pi_i(\mathbf{n}) &= -\frac{\partial}{\partial \theta_i(\mathbf{n})} \left(\phi^\dagger [\mathcal{C}_o^\dagger \mathcal{C}_o]^{-1/2} \phi + S_g(\theta) \right). \end{aligned} \quad (\text{B4})$$

Using another $N'_{\text{pole}} = 20$ pole rational approximation (r'_k, p'_k) for $[\mathcal{C}_o^\dagger \mathcal{C}_o]^{-1/2}$ (which approximates $x^{-1/2}$ within an error of 6×10^{-5} for $x \in [10^{-7}, 1]$), we get the fermionic contribution to the force $d\pi_i/d\tau$,

$$\frac{\partial}{\partial \theta_i(\mathbf{n})} \phi^\dagger [\mathcal{C}_o^\dagger \mathcal{C}_o]^{-1/2} \phi = \sum_{k=1}^{N'_{\text{pole}}} r'_k X_k^\dagger \frac{\partial (\mathcal{C}_o^\dagger \mathcal{C}_o)}{\partial \theta_i(\mathbf{n})} X_k;$$

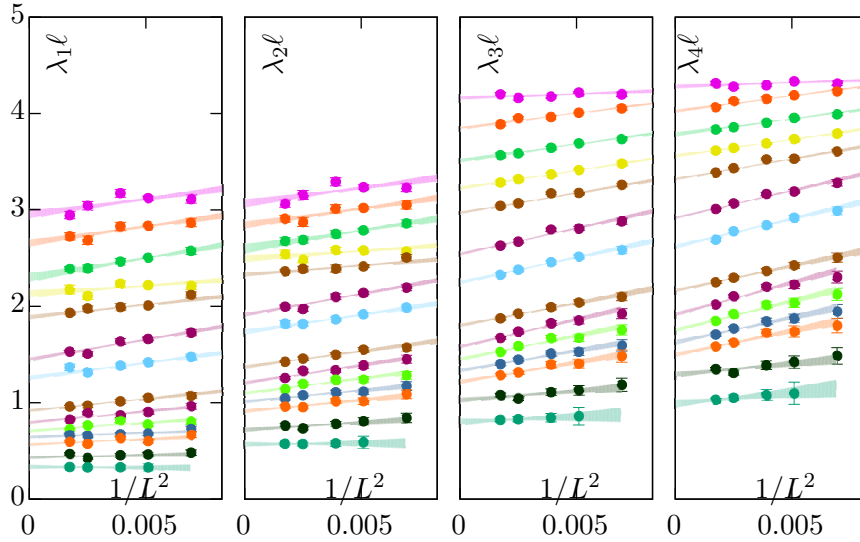


FIG. 7. Continuum extrapolation of the eigenvalues $\lambda_i(\ell; L)\ell$ of $L|G^{-1}|$ for $i = 1, 2, 3, 4$ from the left to right respectively. In each panel, different colored symbols correspond to different fixed ℓ ; from the top to bottom of panels, $\ell = 4, 8, 16, 24, 32, 48.64, 96, 112, 128, 144, 160, 200$ and 250 .

$$X_k = (\mathcal{C}_o^\dagger \mathcal{C}_o + p'_k)^{-1} \phi. \quad (\text{B5})$$

The computation of the rest of the fermionic force calculation for each term in the above sum is the same as the one given in [34].

We evolved each trajectory for 1 unit of time τ ending with an accept/reject step. We tuned the step size $d\tau$ dynamically during runtime such that the acceptance ratio was greater than 80%. After thermalization, we used only configurations separated by 5 trajectories for various measurements reported in this letter. At each simulation point, we collected about 1000 such configurations except in $L = 24$ where the statistics is a bit smaller. The detailed list of simulation points along with the parameters and measurements are given in Table I and Table II.

Appendix C: Measurement of eigenvalues, and the phase \mathcal{A}

For $L = 6, 8, 10, 12, 14$ (and $L = 16$ only for $\ell = 200$), we constructed the unitary matrices $V_\theta, V_{\theta/2}$ explicitly as $2L^3 \times 2L^3$ matrices. Using Lapack subroutines [35], we diagonalized these matrices to obtain their eigenvalues $\exp(i\phi_j)$ and $\exp(i\Phi_j)$ respectively. Using these

eigenvalues, we constructed the phase \mathcal{A} as

$$\mathcal{A} = \text{Im} \log \left(\prod_j^{2L^3} e^{-2i\Phi_j} \prod_k^{2L^3} (1 + e^{i\phi_k}) \right) \in (-\pi, \pi]. \quad (\text{C1})$$

From the eigenvalues $e^{i\phi_j}$ of V_θ , we also obtained the eigenvalues $i\Lambda_j^{-1} = -i \cot(\phi_j/2)$ of the propagator $G(\theta)$. Since the computational cost of the brute force eigenvalue computation is $\mathcal{O}(L^9)$, this was not a feasible method for $L > 14$. Instead, we used Ritz algorithm for $L = 16, 20, 24$ to compute the four low-lying eigenvalues $\cos^2(\phi_j/2)$ of $\mathcal{C}_o^\dagger \mathcal{C}_o$, from which we found the low-lying eigenvalues Λ_j of $|G^{-1}|$.

At finite L , these eigenvalues in lattice units are related to the continuum eigenvalues $\langle \lambda_j \ell \rangle$ through

$$\langle \lambda_j \ell \rangle = 2(M_W - M_t) \langle \Lambda_j \rangle L + \frac{c_1}{L^2} + \dots, \quad (\text{C2})$$

where $M_W - M_t$ is the difference between the mass $M_W (= 1)$ in the Wilson-Dirac Kernel and the mass of the Wilson-Dirac fermion which corresponds to the zero physical mass. We determined M_t as the Wilson mass where the smallest eigenvalue of $\mathcal{C}_W^\dagger \mathcal{C}_W$ is minimized. One should note that $M_t \rightarrow 0$ in the continuum limit and hence the usage of $2(M_W - M_t)$ instead of a simpler $2M_W$ factor was only to improve the approach to the continuum limit. In the main text, the values of $\langle \lambda_j(\ell; L) \rangle \ell$ are connected to the lattice Λ_j through $2(M_W - M_t) \langle \Lambda_j \rangle L$. We have tabulated these values of $\langle \lambda_j(\ell; L) \rangle \ell$ for $j = 1, 2, 3, 4$ for all the simulation points in Table I and Table II. In Figure 7, we show the $1/L^2$ extrapolation of these improved low-lying eigenvalues to their continuum values $\langle \lambda_j \ell \rangle$ using $L = 12, 14, 16, 20$ and 24.

Appendix D: Random matrix theory

The kernel for the random matrix theory appropriate for extracting the condensate, if one exists, is given by [27, 28]

$$K(x, y) = \frac{1}{2} \frac{\sqrt{|xy|}}{x - y} [J_1(\pi x) J_0(\pi y) - J_0(\pi x) J_1(\pi y)]. \quad (\text{D1})$$

The procedure to extract the individual eigenvalue distribution is standard [29]. We obtained the eigenvalues of kernel numerically to a very good accuracy and used them to obtain the individual eigenvalue distributions. The averages of the four lowest distributions that appear in Eq. (9) in the main text are $z_1 = 0.79787$, $z_2 = 1.77186$, $z_3 = 2.763845$ and $z_4 = 3.76384$.

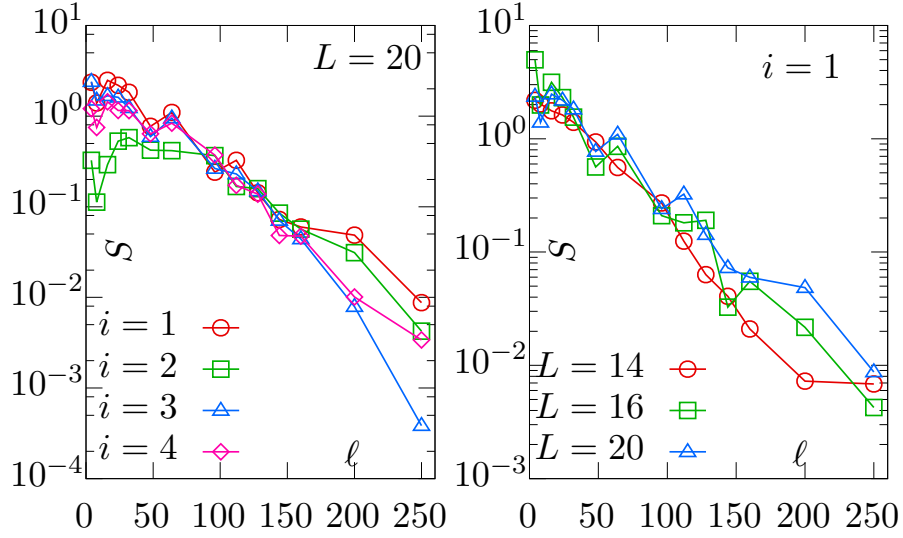


FIG. 8. The square deviation S of data from the RMT model as a function of the physical volume. The ℓ dependences of S for $i = 1, 2, 3, 4$ eigenvalue distributions at a fixed $L = 20$ lattice is shown in the left panel. The lattice spacing effect on the ℓ dependence of S , for fixed $i = 1$, is shown in the right panel.

In Figure 5 of the main text, we compare the distribution P of the i -th scaled Dirac eigenvalue $\ell^2 \Sigma_i \lambda_i$ and the distribution P_{RMT} of i -th eigenvalue from RMT. In order to quantify the approach of the Dirac eigenvalue distribution to the RMT distributions as $\ell \rightarrow \infty$, we consider the sum of square deviations over the $N(= 10)$ bins of the histogram,

$$S = \sum_{z_{\text{bin}}} (P(z_{\text{bin}}) - P_{\text{RMT}}(z_{\text{bin}}))^2. \quad (\text{D2})$$

In the left panel of Figure 8, we show the square deviation S for the four low-lying eigenvalue distributions as a function of ℓ , at fixed $L = 20$. We find S to decrease almost exponentially with ℓ . On the right panel, we show using the distribution of the smallest eigenvalue that the decrease in S with ℓ remains robust as L is increased. Thus, the agreement indeed gets better as one approaches the infinite volume limit for the first four eigenvalues. This is consistent with the presence of a nonzero condensate in the infinite volume limit.

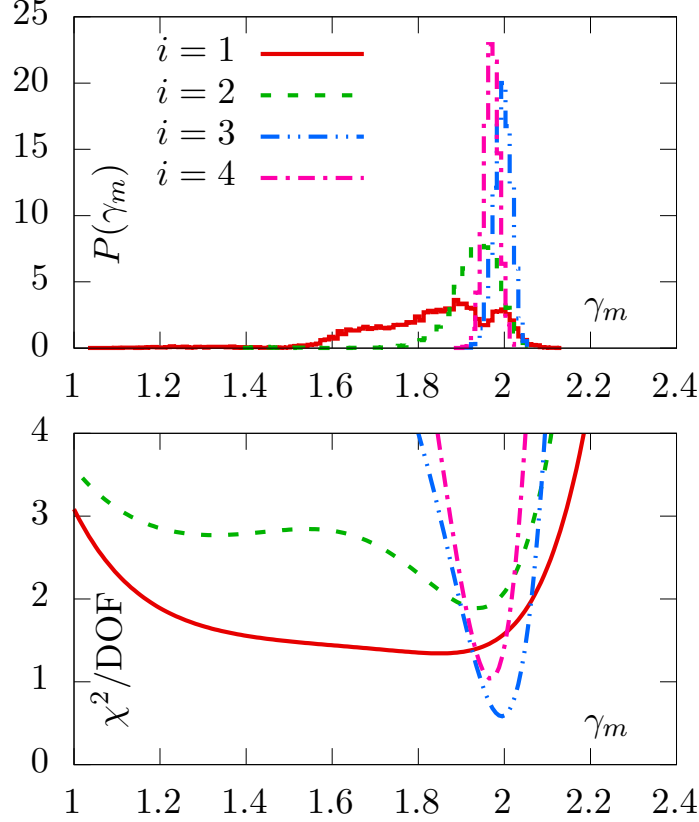


FIG. 9. The χ^2/DOF , a measure of likelihood, of γ_m corresponding to the asymptotic $\Sigma_i(\ell) \sim \ell^{-2+\gamma_m}$ scaling is shown in the bottom panel. The corresponding probability distribution of γ_m , as numerically constructed using best-fit values of γ_m in 5000 different bootstrap samples, is shown in the top panel. The distributions are peaked around $\gamma_m = 2$ corresponding to the symmetry-breaking behavior.

Appendix E: Calculation of \mathbf{J}^q

The essential simplification is

$$2iq^2 \frac{\delta \mathcal{A}_\theta}{\delta \theta_j(\mathbf{n})} = \text{Tr} \left[V_{q\theta}^\dagger \frac{\delta V_{q\theta}}{\delta \theta_j(\mathbf{n})} \right] = \text{ImTr} \left[\frac{1}{C_W} \frac{\delta C_W}{\delta \theta_j(\mathbf{n})} \right], \quad (\text{E1})$$

which is now in terms of the simpler Wilson-Dirac operator. One should also note that the above expression means that the imaginary part of the induced action from both the infinitely massive Wilson-Dirac fermion as well as the corresponding overlap fermion are the same. Thus, all our observations about the Wilson-Dirac operator in [20] hold exactly for overlap fermion as well.

Appendix F: Likelihood of an infra-red fixed point

In the analysis in the main text, we assumed $\Sigma(\ell = \infty) \neq 0$. Instead, if the theory had an infra-red fixed point with a mass anomalous dimension $0 \leq \gamma_m < 2$, then $\Sigma_i(\ell)$ would become zero in the infinite volume with an $\ell^{-2+\gamma_m}$ asymptotic scaling. As a check, we also tried to describe our $\Sigma_i(\ell)$ data using a $\Sigma_i(\ell) = k'_1 \ell^{-2+\gamma_m} (1 + k'_2 \ell^{-1} + k'_3 \ell^{-2})$ ansatz to include corrections to scaling, and we found that χ^2/DOF reaches a minimum, when $\gamma_m \approx 2$. We show this behavior of χ^2 , along with the corresponding bootstrap histogram of γ_m , in Figure 9. Even the lowest eigenvalue that is affected by a soft edge (eigenvalues for a given configuration is not symmetric around zero) shows evidence for a weak minimum for $\gamma \approx 2$. Thus, we find consistent evidences pointing to the presence of parity-breaking bilinear condensate.

-
- [1] M. D. Schwartz, *Quantum Field Theory and the Standard Model* (Cambridge University Press, 2014).
 - [2] L. Alvarez-Gaume and P. H. Ginsparg, Nucl. Phys. **B243**, 449 (1984).
 - [3] W. A. Bardeen and B. Zumino, Nucl. Phys. **B244**, 421 (1984).
 - [4] R. Narayanan and H. Neuberger, Nucl.Phys. **B443**, 305 (1995), arXiv:hep-th/9411108 [hep-th].
 - [5] R. Narayanan and H. Neuberger, Phys. Lett. **B302**, 62 (1993), arXiv:hep-lat/9212019 [hep-lat].
 - [6] S. A. Frolov and A. A. Slavnov, Phys. Lett. **B309**, 344 (1993).
 - [7] D. B. Kaplan, Phys. Lett. **B288**, 342 (1992), arXiv:hep-lat/9206013 [hep-lat].
 - [8] H. Neuberger, Phys. Rev. **D59**, 085006 (1999), arXiv:hep-lat/9802033 [hep-lat].
 - [9] S. Deser, R. Jackiw, and S. Templeton, Annals Phys. **140**, 372 (1982).
 - [10] S. Deser, R. Jackiw, and S. Templeton, Phys.Rev.Lett. **48**, 975 (1982).
 - [11] A. Niemi and G. Semenoff, Phys.Rev.Lett. **51**, 2077 (1983).
 - [12] A. Redlich, Phys.Rev. **D29**, 2366 (1984).
 - [13] L. Alvarez-Gaume, S. Della Pietra, and G. W. Moore, Annals Phys. **163**, 288 (1985).
 - [14] D. T. Son, Phys. Rev. **X5**, 031027 (2015), arXiv:1502.03446 [cond-mat.mes-hall].

- [15] M. A. Metlitski and A. Vishwanath, Phys. Rev. **B93**, 245151 (2016), arXiv:1505.05142 [cond-mat.str-el].
- [16] C. Wang and T. Senthil, Phys. Rev. **B93**, 085110 (2016), arXiv:1507.08290 [cond-mat.str-el].
- [17] Y. Kikukawa and H. Neuberger, Nucl.Phys. **B513**, 735 (1998), arXiv:hep-lat/9707016 [hep-lat].
- [18] R. Narayanan and J. Nishimura, Nucl.Phys. **B508**, 371 (1997), arXiv:hep-th/9703109 [hep-th].
- [19] A. Coste and M. Luscher, Nucl.Phys. **B323**, 631 (1989).
- [20] N. Karthik and R. Narayanan, Phys. Rev. **D92**, 025003 (2015), arXiv:1505.01051 [hep-th].
- [21] A. D. Kennedy, I. Horvath, and S. Sint, *Lattice Field Theory. Proceedings: 16th International Symposium, Lattice '98, Boulder, USA, Jul 13-18, 1998*, Nucl. Phys. Proc. Suppl. **73**, 834 (1999), arXiv:hep-lat/9809092 [hep-lat].
- [22] M. A. Clark and A. D. Kennedy, *Lattice field theory. Proceedings, 21st International Symposium, Lattice 2003, Tsukuba, Japan, July 15-19, 2003*, Nucl. Phys. Proc. Suppl. **129**, 850 (2004), [850(2003)], arXiv:hep-lat/0309084 [hep-lat].
- [23] S. Duane, A. Kennedy, B. Pendleton, and D. Roweth, Phys.Lett. **B195**, 216 (1987).
- [24] M. F. Atiyah and I. M. Singer, Bull. Am. Math. Soc. **69**, 422 (1969).
- [25] C. Callias, Commun. Math. Phys. **62**, 213 (1978).
- [26] T. Banks and A. Casher, Nucl. Phys. **B169**, 103 (1980).
- [27] J. J. M. Verbaarschot and I. Zahed, Phys. Rev. Lett. **73**, 2288 (1994), arXiv:hep-th/9405005 [hep-th].
- [28] P. H. Damgaard and S. M. Nishigaki, Phys. Rev. **D57**, 5299 (1998), arXiv:hep-th/9711096 [hep-th].
- [29] S. M. Nishigaki, *Proceedings, 33rd International Symposium on Lattice Field Theory (Lattice 2015): Kobe, Japan, July 14-18, 2015*, PoS **LATTICE2015**, 057 (2016), arXiv:1606.00276 [hep-lat].
- [30] R. Narayanan and H. Neuberger, Nucl. Phys. **B477**, 521 (1996), arXiv:hep-th/9603204 [hep-th].
- [31] D. F. Mross, J. Alicea, and O. I. Motrunich, Phys. Rev. Lett. **117**, 016802 (2016), arXiv:1510.08455 [cond-mat.str-el].
- [32] M. Cheng and C. Xu, Phys. Rev. **B94**, 214415 (2016), arXiv:1609.02560 [cond-mat.str-el].
- [33] C. Cordova, P.-S. Hsin, and N. Seiberg, (2017), arXiv:1712.08639 [cond-mat.str-el].

- [34] N. Karthik and R. Narayanan, Phys. Rev. **D94**, 065026 (2016), arXiv:1606.04109 [hep-th].
- [35] E. Anderson, Z. Bai, C. Bischof, S. Blackford, J. Demmel, J. Dongarra, J. Du Croz, A. Greenbaum, S. Hammarling, A. McKenney, and D. Sorensen, *LAPACK Users' Guide*, 3rd ed. (Society for Industrial and Applied Mathematics, Philadelphia, PA, 1999).

ℓ	L	$\lambda_1 \ell$	$\lambda_2 \ell$	$\lambda_3 \ell$	$\lambda_4 \ell$	M_t	N_{conf}
4	6	3.296(38)	3.412(39)	4.544(16)	4.649(16)	-0.0048(19)	1008
	8	3.133(57)	3.255(59)	4.327(27)	4.443(26)	-0.0035(22)	1008
	10	3.164(47)	3.287(49)	4.260(17)	4.376(17)	-0.0036(5)	1008
	12	3.112(42)	3.233(43)	4.198(21)	4.312(21)	-0.0033(4)	1008
	14	3.121(21)	3.236(22)	4.217(9)	4.333(9)	-0.0030(3)	2064
	16	3.173(41)	3.293(42)	4.175(15)	4.294(15)	-0.0027(2)	1008
	20	3.043(46)	3.155(47)	4.161(18)	4.280(19)	-0.0023(2)	1008
	24	2.946(38)	3.066(39)	4.198(20)	4.315(19)	-0.0020(2)	528
8	6	3.063(42)	3.235(43)	4.428(16)	4.591(16)	-0.0019(38)	1008
	8	2.897(42)	3.081(45)	4.238(19)	4.410(19)	-0.0035(22)	1008
	10	2.900(51)	3.087(53)	4.101(18)	4.281(18)	-0.0041(12)	1008
	12	2.868(42)	3.052(43)	4.052(16)	4.229(16)	-0.0040(6)	1008
	14	2.836(16)	3.020(17)	4.008(7)	4.189(7)	-0.0041(5)	2736
	16	2.829(43)	3.012(44)	3.964(19)	4.150(19)	-0.0040(5)	1008
	20	2.685(43)	2.874(46)	3.950(17)	4.127(17)	-0.0035(3)	1008
	24	2.727(34)	2.909(34)	3.889(13)	4.065(13)	-0.0032(3)	696
16	6	2.859(37)	3.075(37)	4.160(13)	4.394(12)	0.0131(111)	1008
	8	2.721(33)	2.978(34)	3.922(12)	4.180(11)	0.0075(45)	1008
	10	2.609(31)	2.897(29)	3.820(9)	4.089(9)	0.0024(29)	1008
	12	2.576(35)	2.860(36)	3.734(15)	3.992(15)	-0.0000(19)	1008
	14	2.504(15)	2.788(15)	3.690(7)	3.954(7)	-0.0015(13)	3480
	16	2.464(32)	2.750(34)	3.644(14)	3.903(14)	-0.0023(9)	1008
	20	2.394(32)	2.689(34)	3.586(15)	3.857(14)	-0.0034(6)	1008
	24	2.385(26)	2.676(35)	3.567(19)	3.834(18)	-0.0038(5)	816
24	6	2.718(23)	2.919(23)	3.968(15)	4.253(14)	0.0419(175)	1008
	8	2.534(38)	2.807(34)	3.713(12)	4.018(10)	0.0243(89)	1008
	10	2.390(38)	2.696(35)	3.555(12)	3.872(12)	0.0159(52)	1008
	12	2.208(35)	2.571(36)	3.480(18)	3.791(19)	0.0098(33)	1008
	14	2.219(11)	2.579(11)	3.413(8)	3.735(8)	0.0057(18)	4560
	16	2.234(29)	2.583(28)	3.370(14)	3.691(12)	0.0025(17)	1008
	20	2.107(35)	2.485(33)	3.319(14)	3.643(13)	-0.0004(10)	1008
	24	2.175(15)	2.539(14)	3.285(8)	3.616(8)	-0.0021(5)	936
32	6	2.631(35)	2.798(30)	3.773(16)	4.090(12)	0.0713(242)	1008
	8	2.434(27)	2.688(25)	3.516(12)	3.859(10)	0.0507(122)	1008
	10	2.183(41)	2.502(40)	3.357(12)	3.721(12)	0.0338(81)	1008
	12	2.118(31)	2.507(32)	3.260(19)	3.606(20)	0.0223(46)	1008
	14	2.008(11)	2.413(12)	3.175(12)	3.532(13)	0.0157(34)	4368
	16	1.991(35)	2.391(35)	3.171(14)	3.523(14)	0.0109(23)	1008
	20	1.977(25)	2.389(25)	3.068(13)	3.432(11)	0.0045(13)	1008
	24	1.932(17)	2.363(16)	3.042(9)	3.386(9)	0.0012(8)	984
48	6	2.508(30)	2.596(23)	3.421(11)	3.795(11)	0.1429(369)	1008
	8	2.114(23)	2.371(18)	3.162(12)	3.542(8)	0.1026(219)	1008
	10	1.945(26)	2.280(25)	2.988(11)	3.383(10)	0.0762(136)	1008
	12	1.726(32)	2.193(32)	2.881(30)	3.281(33)	0.0571(90)	1008
	14	1.662(14)	2.140(15)	2.805(18)	3.191(21)	0.0428(61)	3840
	16	1.635(29)	2.098(28)	2.795(17)	3.164(17)	0.0330(42)	1008
	20	1.509(24)	1.973(25)	2.671(14)	3.067(13)	0.0195(23)	1008
	24	1.530(14)	1.996(15)	2.630(10)	3.009(8)	0.0121(14)	984

TABLE I. Simulation parameters ℓ and L , eigenvalue data and statistics N_{conf} .

ℓ	L	$\lambda_1\ell$	$\lambda_2\ell$	$\lambda_3\ell$	$\lambda_4\ell$	M_t	N_{conf}
64	6	2.408(44)	2.378(30)	3.138(13)	3.539(9)	0.2124(526)	1008
	8	1.921(37)	2.140(26)	2.836(11)	3.270(11)	0.1612(288)	1008
	10	1.702(23)	2.000(21)	2.683(10)	3.087(9)	0.1250(178)	1008
	12	1.476(28)	1.988(33)	2.585(38)	2.991(43)	0.0957(127)	1008
	14	1.418(15)	1.917(18)	2.515(21)	2.918(25)	0.0748(77)	3504
	16	1.385(23)	1.864(22)	2.458(18)	2.842(19)	0.0589(54)	1008
	20	1.314(19)	1.816(19)	2.381(14)	2.779(13)	0.0385(31)	1008
	24	1.366(34)	1.820(33)	2.326(19)	2.692(20)	0.0261(20)	984
96	6	2.258(32)	1.961(18)	2.580(11)	2.967(10)	0.3621(689)	1008
	8	1.700(28)	1.779(19)	2.389(10)	2.790(8)	0.2787(402)	1008
	10	1.487(20)	1.670(12)	2.193(9)	2.614(8)	0.2249(261)	1008
	12	1.072(27)	1.573(34)	2.099(41)	2.506(48)	0.1793(155)	1008
	14	1.051(16)	1.550(21)	2.039(27)	2.424(32)	0.1446(111)	2928
	16	1.014(20)	1.497(21)	1.990(23)	2.365(25)	0.1195(83)	1008
	20	0.968(16)	1.458(17)	1.924(15)	2.298(17)	0.0846(55)	1008
	24	0.962(10)	1.424(13)	1.876(12)	2.249(12)	0.0605(32)	768
112	12	0.963(29)	1.451(41)	1.924(52)	2.303(62)	0.2187(206)	1008
	14	0.903(19)	1.385(27)	1.853(36)	2.227(43)	0.1831(156)	2640
	16	0.869(19)	1.338(22)	1.824(23)	2.201(27)	0.1500(96)	1008
	20	0.893(14)	1.333(16)	1.737(16)	2.103(18)	0.1089(65)	1008
	24	0.822(11)	1.255(12)	1.670(11)	2.018(13)	0.0811(37)	672
128	12	0.802(27)	1.285(39)	1.755(52)	2.125(62)	0.2631(214)	1008
	14	0.775(20)	1.241(29)	1.673(39)	2.036(47)	0.2175(180)	2280
	16	0.814(18)	1.238(22)	1.671(26)	2.015(31)	0.1800(118)	1008
	20	0.764(14)	1.195(17)	1.587(18)	1.920(20)	0.1335(80)	1008
	24	0.722(12)	1.139(13)	1.526(13)	1.848(13)	0.1010(49)	600
144	12	0.727(30)	1.173(45)	1.594(60)	1.946(72)	0.3044(257)	1008
	14	0.679(18)	1.115(28)	1.528(37)	1.873(46)	0.2524(181)	2016
	16	0.670(17)	1.108(22)	1.511(27)	1.844(33)	0.2127(132)	1008
	20	0.658(13)	1.077(14)	1.446(17)	1.768(20)	0.1587(84)	1008
	24	0.666(11)	1.046(13)	1.400(13)	1.708(15)	0.1226(59)	600
160	12	0.668(30)	1.088(46)	1.483(63)	1.801(75)	0.3389(275)	1008
	14	0.603(21)	1.016(34)	1.406(46)	1.739(57)	0.2880(233)	1870
	16	0.631(18)	1.017(25)	1.397(32)	1.723(38)	0.2450(163)	1008
	20	0.575(12)	0.954(15)	1.314(18)	1.624(21)	0.1846(96)	1008
	24	0.596(10)	0.959(13)	1.286(13)	1.582(13)	0.1437(56)	480
200	12	0.481(29)	0.842(49)	1.186(68)	1.486(85)	0.4256(329)	1008
	14	0.464(22)	0.808(37)	1.128(51)	1.423(63)	0.3733(276)	1008
	16	0.455(16)	0.780(25)	1.109(35)	1.389(43)	0.3206(204)	1008
	20	0.428(11)	0.733(16)	1.043(20)	1.310(24)	0.2491(126)	983
	24	0.467(14)	0.764(15)	1.078(18)	1.348(18)	0.1958(90)	359
250	14	0.329(35)	0.590(62)	0.860(90)	1.098(115)	0.4614(563)	1008
	16	0.330(17)	0.578(29)	0.846(42)	1.082(54)	0.4153(285)	1007
	20	0.329(11)	0.571(17)	0.828(23)	1.051(29)	0.3248(177)	1006
	24	0.333(10)	0.575(11)	0.822(15)	1.031(16)	0.2616(94)	240

TABLE II. Simulation parameters ℓ and L , eigenvalue data and statistics N_{conf} .